scientific reports

Check for updates

OPEN

Zinc complex with quinoline-based thiazolyl-hydrazone targeting DNA replication in cancer cells

Natalia Maciejewska[1]✉, Jovana Araškov[2], Mateusz Olszewski[1], Aleksandar Višnjevac[3], Nenad Filipović[4], Magdalena Stevanović[4], Berta Barta Holló[5], Tamara Todorović[2] & Nenad Filipović[6]✉

The development of selective anticancer agents remains a central objective in medicinal chemistry. Here, we report the synthesis, structural characterization, and biological evaluation of the first metal complex of a quinoline-based thiazolyl-hydrazone ligand [(*E*)-2-(8-(quinolin-2-ylmethylene)hydrazinyl)-4-(4-tolyl)-1,3-thiazole)] (HL). Obtained octahedral Zn(II) complex $[Zn(HL)_2](NO_3)_2$, (1), is based on two *NNN* tridentate coordinated ligands. In vitro cytotoxicity assays revealed that the complex exhibits potent and selective activity against lung adenocarcinoma A-549 and colorectal carcinoma HCT-116, while sparing non-tumorigenic human embryonic kidney HEK-293 cells. Mechanistic studies demonstrated that the complex induces S-phase arrest, inhibits DNA synthesis, and triggers significant DNA damage as indicated by increased p-γH2AX expression. These effects were accompanied by mitochondrial depolarization, caspase-3/7 activation, and phosphatidylserine externalization, confirming apoptosis via the intrinsic pathway. The compound further inhibited tumor growth in 3D spheroids and the chick chorioallantoic membrane model without overt toxicity. Compared to the free ligand and reference chemotherapeutics, the zinc complex showed improved efficacy and selectivity. These results highlight the potential of metal coordination to enhance the biological activity of hybrid ligands, supporting further development of this class of compounds as selective anticancer agents.

Keywords Apoptosis, Anticancer activity, DNA damage, Hydrazonyl-thiazoles, Quinoline derivatives

The continued search for effective and selective anticancer agents remains a significant challenge in medicinal chemistry. Despite the development of targeted therapies and immunotherapeutics, many cancers—especially solid tumors—still exhibit resistance, limited response durability, and off-target toxicities. The emergence of drug resistance, heterogeneity of tumor microenvironments, and limited tumor selectivity of current chemotherapeutics underscore the urgent need for new chemical entities that not only disrupt cancer cell viability but also spare healthy tissues. Rational drug design strategies that incorporate well-characterized pharmacophores into multifunctional hybrid molecules, along with their coordination with biologically relevant metals, represent a promising approach to addressing these limitations.

Thiazole and hydrazone moieties are recognized as privileged scaffolds in the development of bioactive molecules, including anticancer agents. To date, the U.S. Food and Drug Administration (FDA) has approved 26 thiazole-based drugs, of which five are cytostatics. In parallel, five hydrazone-based drugs have reached the market, with three others currently undergoing cancer-related clinical trials[1]. Their hybrid derivatives—thiazolyl-hydrazones (THs)—exhibit the ability to interact with a wide array of biologically relevant targets implicated in cancer progression, including histone acetyltransferases[2], alkaline phosphatases[3], vimentin[4], cyclooxygenase-2[5], matrix metalloproteinases 2 and 9[6], aldose reductase[7], α-amilase[8], β-glucuronidase[9], ecto-5′-nucleotidase[10], ribonucleotide reductase[11], eukaryotic initiation factor 4E[12], tubulin[13], aromatase[14], monoamine oxidases A and B[15], cholinesterases[16], and several oncogenic kinases including Akt, HER-2, EGFR, VEGFR, BRAFV 600 E,

[1]Department of Pharmaceutical Technology and Biochemistry, Faculty of Chemistry, Gdansk University of Technology, Narutowicza St 11/12, 80-233 Gdansk, Poland. [2]Faculty of Chemistry, University of Belgrade, Studentski trg 12-16, Belgrade 11000, Serbia. [3]Division of Physical Chemistry, Institute Ruđer Bošković, Bijenička cesta 54, 10000 Zagreb, Croatia. [4]Group for Biomedical Engineering and Nanobiotechnology, Institute of Technical Sciences of SASA, Kneza Mihaila 35/IV, Belgrade 11000, Serbia. [5]University of Novi Sad-Faculty of Sciences, Trg Dositeja Obradovića 4, Novi Sad 21000, Serbia. [6]Faculty of Agriculture, University of Belgrade, Nemanjina 6, Belgrade 11000, Serbia. ✉email: natalia.maciejewska@pg.edu.pl; nenadf@agrif.bg.ac.rs

PI3K, CDK2, and tyrosinase[4,5,14,16–20]. This pharmacological versatility underscores their therapeutic potential in the development of cancer drugs.

Similarly, quinoline has been extensively investigated as a core pharmacophore in oncology and other therapeutic areas. The FDA has approved twenty-one quinoline-based drugs, while several others are undergoing clinical trials for cancer treatment[1]. Hybrid molecules incorporating quinoline with hydrazone[21–23] or thiazole moieties[24,25] have also demonstrated promising bioactivities. Moreover, coordination of these hybrid ligands with transition metals—particularly redox-inactive ones—can further enhance their anticancer properties through mechanisms such as improved cellular uptake, altered biodistribution, or synergistic targeting[26–28].

Despite the growing interest in hybrid structures, compounds simultaneously incorporating quinoline, thiazole, and hydrazone motifs—referred to as quinoline-based thiazolyl-hydrazones (QTHs)—remain poorly studied. To our knowledge, only a handful of studies have investigated the biological activities of QTHs[1,25]. For instance, Evren et al. reported antifungal and anticandidal effects of 3-quinoline THs[25], while Erguç et al. synthesized 4-quinoline THs and observed antiproliferative effects, though without elucidating their mechanisms of action[29]. Our prior work identified ((*E*)-2-(2-(quinolyl-8-ol-2-ylmethylene)hydrazinyl))-4-(4-methoxyphenyl)-1,3-thiazole as the most promising QTH derivative within the library of invetigated QTHs, exhibiting potent cytotoxic activity against A-549 (lung adenocarcinoma), HCT-116 (colorectal carcinoma), MCF-7 (breast adenocarcinoma), U-2 OS (osteosarcoma), and Hep G-2 (hepatocarcinoma) cell lines. In particular, this compound showed the highest potency and was found to inhibit autophagy as its primary mechanism of action[1]. In contrast, QTH analogues lacking the hydroxyl substituent, such as compound ((*E*)-2-(8-(quinolin-2-ylmethylene)hydrazinyl)-4-(4-tolyl)-1,3-thiazole) (**HL**) (Fig. 1), were biologically inactive in these models[1].

A promising strategy to improve the activity and selectivity of such hybrid ligands lies in metal coordination. Among metal-based systems, zinc stands out as an attractive, non-toxic, and abundant element with a broad range of physiological roles. Zinc is the second most prevalent trace metal in the human body and plays essential roles in DNA synthesis, antioxidant defense, immune function, cellular proliferation, and apoptosis. Its biochemical relevance and low systemic toxicity have positioned zinc complexes as a compelling class of metal–drug conjugates for therapeutic applications[30,31]. A recent review by Biswas et al. highlighted the anticancer potential of zinc complexes, particularly those functioning as carriers for bioactive ligands with intrinsic pharmacological activity[32]. These complexes can facilitate targeted drug delivery while modulating cellular uptake and metabolism.

In our recent studies, we demonstrated that the coordination of pyridine-based THs to zinc ions resulted in a marked increase in cytotoxicity, even in cases where the free ligands were inactive[33,34]. Encouraged by these findings, we aimed to extend this strategy to the largely unexplored class of QTHs. The goal of this study was to prepare and characterize the first zinc complex of a QTH ligand and to investigate its antiproliferative properties and mechanism of action thoroughly. Herein, we report the synthesis of a zinc(II) complex (**1**) with ligand **HL**, and provide a comprehensive biological evaluation using multiple cancer cell models. Through a series of cellular, molecular, and in ovo experiments, we investigate the cytotoxic, proapoptotic, and antitumor properties of this novel complex, providing insights into its mechanism of action and potential as a selective anticancer agent.

Results

Chemistry

The complex (**1**) was synthesized by reaction of ligand **HL** and $Zn(NO_3)_2{\cdot}4H_2O$ in methanol. Elemental analysis confirmed the composition and purity of the final product. The structure of complex **1** was determined by single crystal X-ray diffraction (XRD) analysis, and further confirmed by solid-state IR and UV-Vis spectroscopy. The characterization of complex **1** in the solution was performed using UV-Vis and NMR spectroscopy. Moreover,

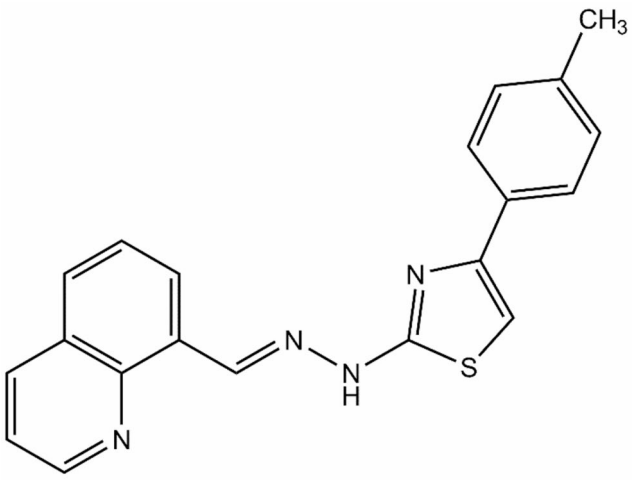

Fig. 1. Chemical structure of ligand **HL**.

characterization of complex **1** in solution was further performed by molar conductivity measurements. Comparative analysis of the IR spectra of the ligand **HL** and the complex **1** (see Supplementary Figs. S1 and S2) confirmed ligand coordination to the Zn(II) ion. In the complex, a medium-intensity band observed at 3082 cm^{-1} was assigned to the hydrazone N–H stretch[35], indicating that the ligand coordinates in its neutral form. The presence of two strong absorption bands at 1380 and 1327 cm^{-1} corresponds to nitrate ions in the other sphere of the complex[36]. The solid state UV–Vis spectra of ligand **HL** and complex **1** are very similar, showing two strong absorption maxima around 280 and 400 nm (see Supplementary Fig. S3). This observation may indicate that only intra-ligand (IL) and ligand-to-ligand charge transfer (LLCT) processes occur, which is consistent with the behavior previously reported for nitrate Zn(II) complexes with pyridine-based THs[33]. The UV–Vis spectra of ligand **HL** and complex **1** recorded in dimethylsulfoxide (DMSO), both displaying two absorption bands at ca. 285 and 385 nm (see Supplementary Fig. S4). The similarity between the solution and solid-state spectra further supports the dominance of IL and LLCT transitions, suggesting that coordination to the Zn(II) ion has no influence on the ligand-centered electronic transitions.The ^{1}H and ^{13}C NMR spectra of the complex **1** (see Supplementary Figs. S5 and S6) displayed a single set of signals, consistent with the presence of only one form of the complex in solution. Notably, the ^{1}H NMR spectrum exhibits a signal at approximately 12.40 ppm, corresponding to the N–H proton, further supporting coordination of the ligand in its protonated form. No significant chemical shift changes were observed in the proton and carbon signals between the spectra of ligand **HL** and complex **1**. This behavior is consistent with previously reported Zn(II) complexes bearing pyridine-based THs[33] and thiosemicarbazone ligands[37]. Molar conductivity measurements in DMSO solution indicated that the complex behaves as a 2:1 electrolyte, and its conductivity remains unchanged over a 24 h. Based on those mentioned above and the XRD study (vide infra), the molecular formula of the investigated Zn(II) complex (**1**) is $[Zn(HL)_2](NO_3)_2$.

Single-crystal analysis

Single crystals suitable for XRD analysis were obtained directly from the mother liquor. The complex crystallized in the monoclinic $P2_1/c$ space group. XRD analysis revealed that the Zn(II) center adopts a distorted octahedral coordination geometry with bond lengths between 2.094(4) and 2.221(5) Å (see Supplementary Table S1) and bond angles between 76.09(17) and 175.28(17)° (see Supplementary Table S2). Two neutral tridentate ligands are coordinated through the quinoline, imine, and thiazole nitrogen atoms, forming one six-membered and one five-membered chelate ring. The crystal structure is completed by the presence of two nitrate anions located in the outer coordination sphere (Fig. 2).

The intermolecular interactions in the crystal packing of complex **1** were initially analyzed using a conventional atom-to-atom crystallographic approach (Table 1). The structure is primarily stabilized by hydrogen and π···π stacking interactions. The complex cation forms hydrogen interactions with four adjacent nitrate anions. Two of these interactions are bifurcated classical hydrogen interactions, where the imine nitrogens act as donors and nitrate oxygens act as acceptors. Additionally, the formation of two non-classical hydrogen interactions through the quinoline carbon atoms as donors resulting in a *zig-zag* 1D chain along the *c* crystallographic axis (Fig. 3, interaction marked as green dashed lines). Each complex cation from the 1D chain is involved in four π···π interactions with complex cations from the adjacent chains through quinoline and tolyl rings, forming a 2D layer parallel to the *bc* crystallographic plane (Fig. 3, interaction marked as red dashed lines). Further, 2D layers are connected *via* four non-classical hydrogen interactions, where complex cations are donors in these interactions through quinoline and thiazole carbon atoms, while oxygen atoms from neighboring NO_3^- anions represent acceptors.

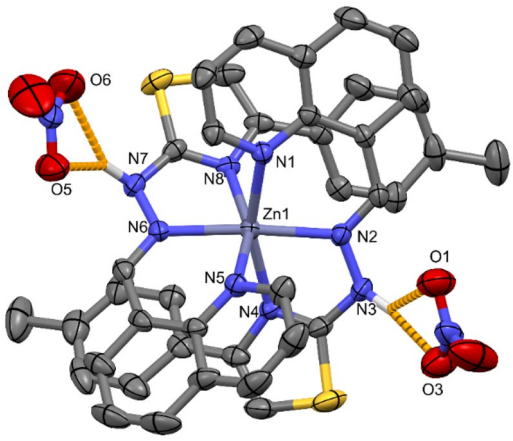

Fig. 2. ORTEP plot of the molecular structure of complex **1** with hydrogen interactions outlined. For clarity, thermal ellipsoids are given at the 30% probability level and all hydrogen atoms are omitted, with the exception of those involved in hydrogen bonding.

Interactions parameters				
Hydrogen interactions parameters				
N–H···A	**H···A (Å)**	**D···A (Å)**	**D-H···A (°)**	**sym. op. on A**
N3–H3A···O1	2.30	3.004(10)	125	x, y,z
N3–H3A···O3	1.83	2.838(9)	169	x, y,z
N7–H7A···O5	2.01	2.867(1)	141	x, y,z
N7–H7A···O6	2.16	3.087(11)	152	x, y,z
C3–H3···O4	2.41	3.377(13)	148	1-x,-y,1-z
C7–H7···O5	2.58	3.526(10)	144	x,1/2-y,1/2 + z
C9–H9···O4	2.43	3.388(14)	147	1-x,-y,1-z
C13–H13···O2	2.20	3.166(11)	146	2-x,1/2 + y,3/2-z
C27–H27···O2	2.56	3.456(13)	139	x,1/2-y,-1/2 + z
C33–H33···O6	2.42	3.465(11)	161	1-x,1-y,1-z

Aromatic cycle stacking parameters						
Ω(I), Ω(J)[A]	**Cg···Cg[B] (Å)**	**α[C] (°)**	**β[D] (°)**	**γ[E] (°)**	**Slippage[F] (Å)**	**Symmetry operation on J**
Cg1,Cg4	3.659(4)	3.4(3)	1.5	1.9	0.095	x,-1 + y, z
Cg4,Cg1	3.659(4)	3.4(3)	1.9	1.5	0.123	x,1 + y, z
Cg2,Cg3	3.709(4)	6.2(3)	18.3	12.1	1.162	x,1 + y, z
Cg3,Cg2	3.709(4)	6.2(3)	12.1	18.3	0.777	x,-1 + y, z

Table 1. Crystal packing parameters in the crystal structures of complex **1**. [A]Planes of the rings I, J: ring Ω(1) = N1–C1–C2–C3–C4–C5–C6–C7–C8–C9; Ω(2) = C14–C15–C16–C17–C18–C19; Ω(3) = N5–C21–C22–C23–C24–C25–C26–C27–C28–C29; Ω(4) = C34–C35–C36–C37–C38–C39. [B]Cg···Cg = distance between ring centroids. [C]α = dihedral angle between planes I and J. [D]β = angle between Cg(I)→Cg(J) vector and normal to plane I. [E]γ = angle between Cg(I)→Cg(J) vector and normal to plane J. [F]Slippage = distance between Cg(I) and the perpendicular projection of Cg(J) on ring I.

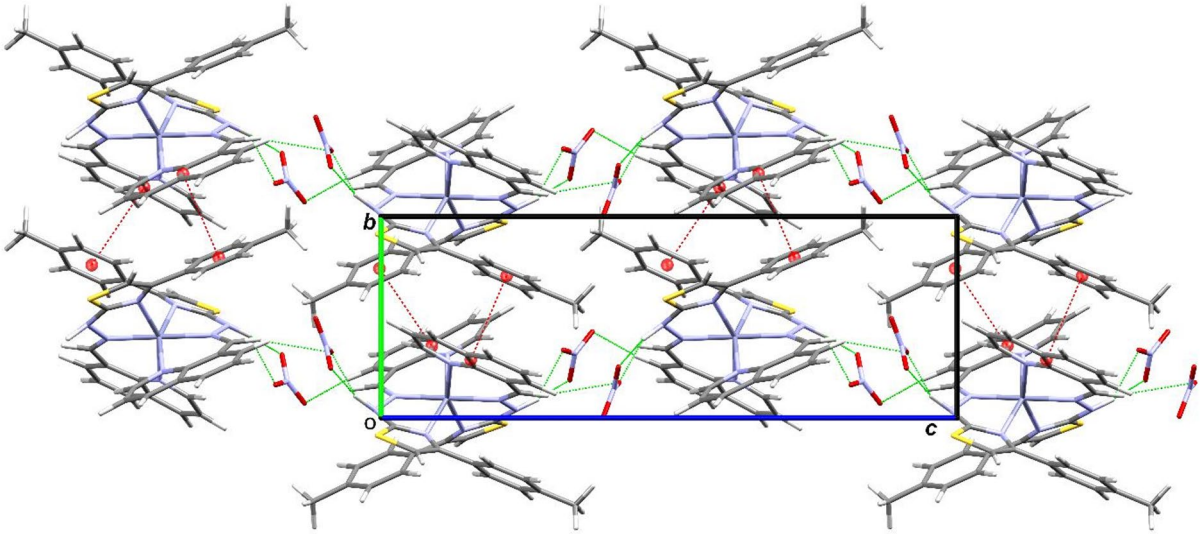

Fig. 3. 2-D layers parallel to the *bc* crystallographic plane in the crystal structure of complex **1**.

Thermal properties of 1

The thermal stability of complex **1** was analyzed by simultaneous thermoanalytical technique, thermogravimetry-differential scanning calorimetry (TG-DSC) in argon. It remains stable up to 251 °C, upon heating (Fig. 4). Such high thermal stability suggests that the intermolecular interactions inside the crystal lattice of the compound are strong. Above the onset temperature, only one mass loss step of complex **1** can be distinguished, with a DTG maximum at 272 °C and a mass decrease of 22%. Above 300 °C, the decomposition rate slows down, and the decomposition processes are almost completely overlapped. Only two slight DTG peaks can be observed at 331 and 363 °C. The thermal degradation of complex **1** does not occur above 700 °C.

The only precepted degradation step of complex **1** is followed by an exothermic heat effect with a peak maximum at 274 °C. The exothermicity of this step was expected due to the presence of nitrate counterions. Due

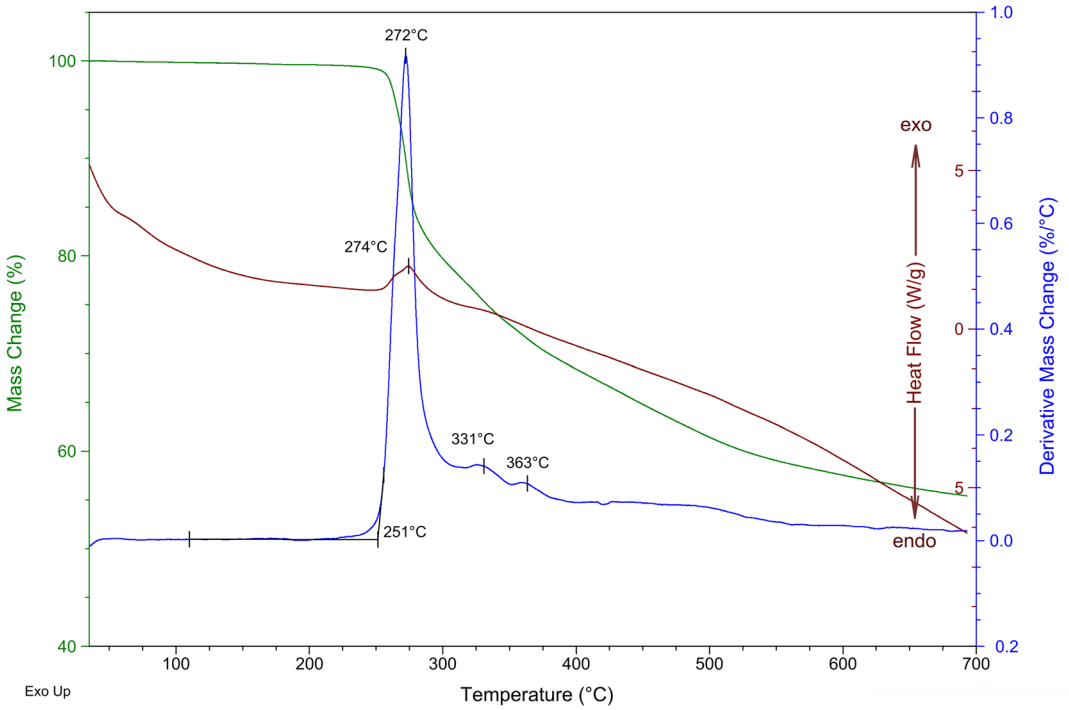

Fig. 4. TG, DTG, and DSC curves of complex **1** in argon.

Cell line	HL	1	5-FU	ETP
	IC_{50} [μM]			
A-549	21.06 ± 2.09	5.24 ± 1.18	8.32 ± 1.11	0.54 ± 0.21
HCT-116	> 50	3.92 ± 0.28	5.24 ± 0.22	0.39 ± 0.01
MCF-7	> 50	> 50	8.31 ± 0.88	0.83 ± 0.15
U-2 OS	> 50	> 50	13.11 ± 0.08	0.61 ± 0.04
HEK-293	> 50	> 50	10.44 ± 0.95	1.91 ± 0.97
SI	> 2.3	> 11	1.2	3.2

Table 2. Half-maximal inhibitory concentration (IC_{50}) values [μM] for ligand **HL** and complex **1** determined in A-549, HCT-116, MCF-7, U-2 OS, and HEK-293 cells after 72-h treatment. IC_{50} values were calculated based on nonlinear regression of dose–response data from three independent experiments. Estimated selectivity indices (SI), calculated as the ratio of IC_{50} in HEK-293 to IC_{50} in cancer cells, are also shown.

to its high oxygen content, the thermal decomposition of nitrate is usually accompanied by intramolecular redox processes and an exothermic heat effect.

The results of coupled TG with mass spectrometry measurements confirmed the expected oxidation processes caused by the nitrate, as evidenced by the evolution of water (m/z 18 and 17), NO, and N_2O (m/z 30 and 44). The other detected fragments, with m/z values of 14, 16, 27, 28, 29, 32, and 39, indicate degradation of ligand **HL** (see Supplementary Fig. S7).

Selective cytotoxic activity of 1 toward lung and colon cancer cells

To investigate the anticancer potential of complex **1**, a cytotoxicity assessment was conducted using the MTT assay following a 72-h incubation. The study involved four human cancer cell lines—A-549, HCT-116, MCF-7, and U-2 OS—as well as one non-tumorigenic cell line, HEK-293 (human embryonic kidney). For comparison reasons, ligand **HL** and two reference chemotherapeutics, etoposide (**ETP**) and 5-fluorouracil (**5-FU**), were also subjected to these investigations.

As previously reported, ligand **HL** exhibited selective cytotoxic activity only in A-549 cells, with an estimated IC_{50} of ~ 21 μM[1], and was inactive in the remaining cancer models as well as in HEK-293 cells, suggesting a limited but selective activity profile (Table 2).

In contrast, complexation with Zn(II) into complex **1** markedly enhanced biological activity (Table 2; Fig. 5). In A-549 cells, **(1)** exhibited a 5.25-fold increase in cytotoxicity compared to ligand **HL**, confirming the beneficial effect of metal coordination. Additionally, complex **1** became active against HCT-116 cells, with an IC_{50} value of

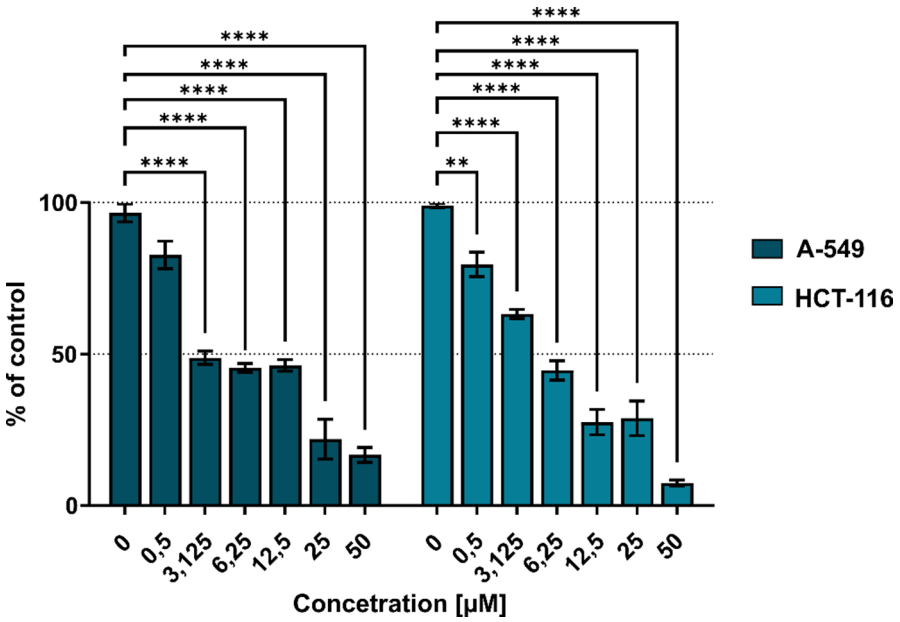

Fig. 5. Cytotoxic activity of the complex **1** in human cell lines. Dose–response curves showing the effect of increasing concentrations of complex **1** on cell viability, as assessed by MTT assay. Data are presented as mean ± SD from three biological replicates.

5.24 ± 1.18 μM (Table 2). Importantly, the compound remained inactive in MCF-7, U-2 OS, and HEK-293 cells, underscoring its selective cytotoxicity toward specific cancer types.

To benchmark the activity and selectivity of ligand **HL** and complex **1**, we compared them with **ETP** and **5-FU**. Both reference drugs were cytotoxic across all cancer cell lines tested but also significantly affected HEK-293 cells, resulting in lower selectivity (Table 2). While selectivity indices (SI; ratio of IC_{50} in non-cancerous to cancerous cells) were not formally calculated for ligand **HL** and complex **1**, they could be estimated to exceed 2.3 for ligand **HL** and 11.0 for complex **1**. In contrast, **5-FU** and **ETP** showed SI values of only 1.2 and 3.2, respectively, indicating less selective toxicity toward cancer cells (Table 2).

A clear dose-dependent cytotoxic response was observed for complex **1** in both A-549 and HCT-116 cells, as shown in Fig. 5. Increasing compound concentrations resulted in a progressive reduction in cell viability, confirming a concentration-dependent mechanism. Meanwhile, **HL**, **ETP**, and **5-FU** induced more uniform cytotoxicity across cell lines, without notable sparing of the non-cancerous model (Table 2).

Altogether, these findings indicate that metal complexation markedly enhances the cytotoxic potency of ligand **HL** and confers improved cancer cell selectivity. Compared to standard chemotherapeutics, complex **1** demonstrates a more favorable activity profile, suggesting its potential as a targeted anticancer agent and warranting further investigation into its molecular mechanism of action. Therefore, all subsequent mechanistic cellular studies in this work were performed in the HCT-116 model, which was selected as the most responsive cancer cell line to complex **1**.

Complex 1 halts cell cycle progression in S phase

To further investigate the mechanism of cytotoxicity induced by complex **1**, we assessed its impact on the cell cycle distribution and DNA synthesis in HCT-116 cells using flow cytometry (Fig. 6). The untreated control cells exhibited a typical DNA content profile, with the majority of cells in the G_0/G_1 phase and smaller proportions in the S and G_2/M phases, reflecting normal proliferation dynamics (Fig. 6a). Upon treatment with complex **1**, a marked and concentration-dependent accumulation of cells in the S phase was observed, accompanied by a corresponding decrease in the G_0/G_1 population (Fig. 6a,b). This redistribution suggests that complex **1** interferes with DNA replication, leading to arrest during the S phase. The G_2/M fraction remained relatively unchanged, indicating that the dominant effect was on S phase progression rather than mitotic entry. Quantitative analysis confirmed this trend: the proportion of S-phase cells increased from approximately 25% in the control to nearly 46% upon treatment with complex **1** (Fig. 6b). To validate the reliability of the assay, **ETP** was included as a positive control. As expected from previously published data, **ETP** treatment resulted in a significant accumulation of cells in the G_2/M phase, confirming the assay's sensitivity in detecting compound-specific cell cycle alterations (Fig. 6a,b)[37].

To confirm whether the observed S-phase accumulation following treatment with complex **1** reflected impaired DNA synthesis rather than increased replication activity, we performed 5-bromo-2′-deoxyuridine (BrdU) incorporation assays. BrdU is a thymidine analog that is incorporated into newly synthesized DNA and serves as a direct marker of active replication[38]. As shown in the representative histograms (Fig. 6c,d), treatment with 25 μM of complex **1** significantly reduced BrdU incorporation, with only 10.2% ± 3.2 of cells testing positive compared to the untreated control ($p < 0.001$). This reduction confirms that the S-phase arrest is associated with

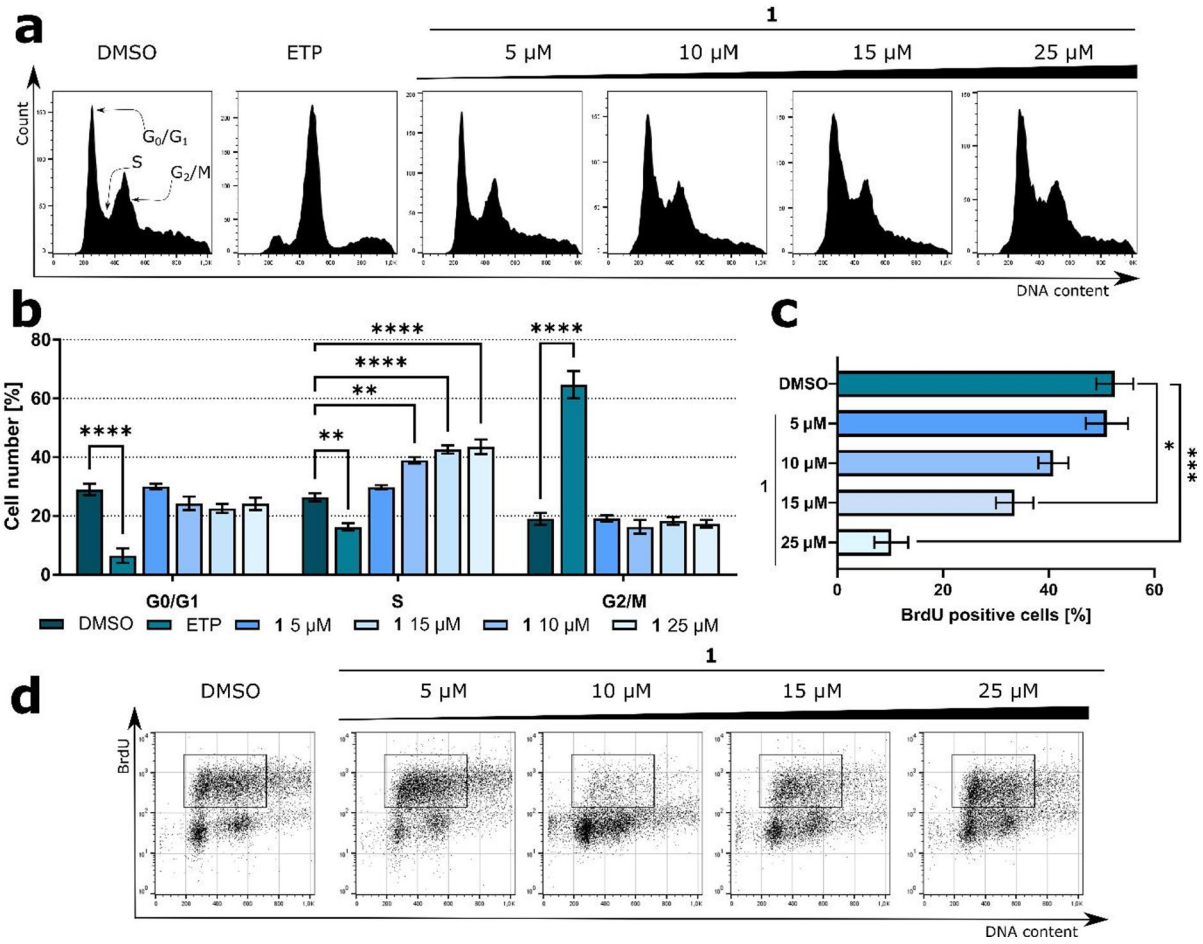

Fig. 6. Flow cytometric analysis of cell cycle distribution and DNA synthesis in HCT-116 cells following treatment with complex **1** and **ETP**. (**a**) Representative DNA content histograms of propidium iodide-stained cells after 48 h treatment. (**b**) Quantification of cell cycle phases (G_0/G_1, S, G_2/M) presented as bar graphs. (**c**) BrdU incorporation assay: quantification of BrdU-positive cells following 48 h treatment with complex **1**, shown as a percentage of the total cell population. (**d**) Representative BrdU histograms corresponding to the quantification in (**c**). Error bars represent mean ± SD from three independent experiments. Statistical significance was assessed using one-way ANOVA followed by Dunnett's post hoc test. $^{*}p < 0.01$, $^{**}p < 0.001$, $^{***}p < 0.0001$, $^{****}p < 0.00001$ vs. vehicle-treated control.

inhibition of DNA synthesis. Collectively, these findings demonstrate that complex **1** exerts its cytotoxic effect, at least in part, by inducing replication stress and causing a robust S-phase arrest in HCT-116 cells.

Assessment of DNA damage response via γH2AX expression in complex 1-treated cells

To further investigate whether the S-phase arrest induced by complex **1** is associated with replication stress and DNA damage, we assessed the levels of phosphorylated histone H2AX (γH2AX), a well-established marker of DNA double-strand breaks. HCT-116 cells were treated with increasing concentrations of complex **1**, and the extent of DNA damage was quantified by flow cytometric analysis of γH2AX-positive cells. As shown in the representative dot plots and summarized in the bar chart (Fig. 7a,b), treatment with complex **1** resulted in a significant and dose-dependent increase in the γH2AX-positive population compared to the untreated control. At the highest tested concentration (25 μM), the proportion of γH2AX-positive cells reached approximately 75%, whereas in control samples the baseline γH2AX signal was negligible.

This increase in γH2AX levels suggests that complex **1** induces substantial DNA damage, likely as a result of stalled or collapsed replication forks during S phase. The elevated levels of DNA damage are consistent with the previously observed block in BrdU incorporation and cell cycle arrest, and they support the hypothesis that replication stress is a central component of the cytotoxic mechanism of this compound. Notably, the level of γH2AX induction by complex **1** was comparable to or even exceeded that observed for **ETP**, which served as a positive control and is known to induce DNA double-strand breaks via topoisomerase II inhibition.

To further validate these findings and visualize the spatial distribution of DNA damage, we performed confocal laser scanning microscopy of HCT-116 cells stained for p-γH2AX, F-actin, and nuclei (4′,6-diamidyno-2-fenyloindol; DAPI) following 48-h treatment. As shown in Fig. 8, control cells (DMSO-treated) displayed uniformly stained nuclei with minimal p-γH2AX signal and intact cortical F-actin structures. In contrast, **ETP**-

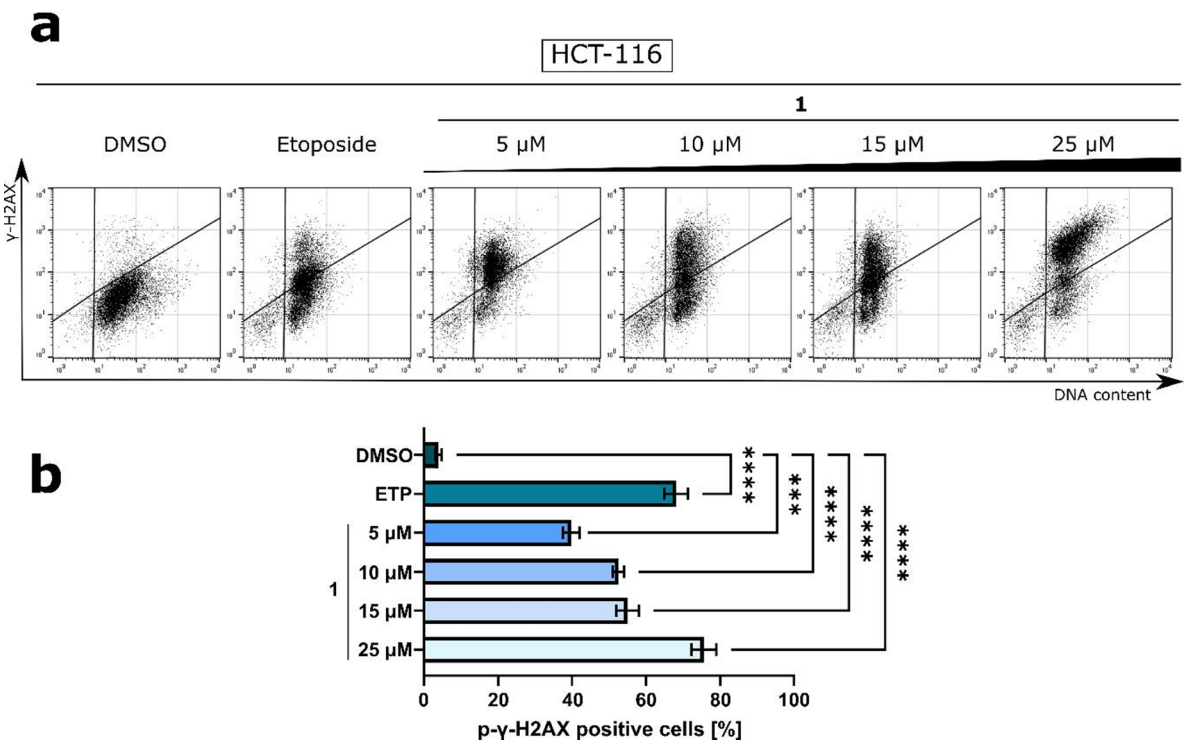

Fig. 7. Induction of DNA damage in HCT-116 cells following treatment with complex **1**. (**a**) Representative flow cytometry dot plots showing phosphorylated γH2AX (p-γH2AX) expression in HCT-116 cells after 48-h treatment with complex **1**, **ETP** (positive control), or DMSO (vehicle). (**b**) Quantitative analysis of the percentage of p-γH2AX–positive cells. Data are presented as mean ± SEM from three independent experiments ($n = 3$). Statistical significance was determined using two-way ANOVA followed by Dunnett's post hoc test. $^{****}p < 0.0001$ vs. vehicle-treated control.

treated cells exhibited intense nuclear p-γH2AX foci formation, consistent with its genotoxic activity. Notably, treatment with complex **1** resulted in a similar pattern of p-γH2AX accumulation, with pronounced intranuclear foci indicating the presence of double-strand breaks. Moreover, in cells treated with higher concentrations of complex **1**, subtle alterations in F-actin organization were observed, including reduced fiber density and cell rounding, suggesting that extensive DNA damage may initiate cytoskeletal remodeling, a phenomenon often associated with stress responses, impaired adhesion, or early stages of apoptosis (Fig. 8).

Together, these results provide strong and complementary evidence—both quantitative and morphological—that complex **1** causes replication-associated DNA damage in HCT-116 cells. The induction of γH2AX, confirmed by both flow cytometry and high-resolution confocal imaging, reinforces the proposed mechanism of action involving replication stress, cell cycle disruption, and impaired DNA synthesis.

Complex 1 induces mitochondria-dependent apoptotic cell death

To investigate the mechanism of cell death induced by complex **1**, we performed flow cytometric assays to assess phosphatidylserine externalization, mitochondrial membrane potential (ΔΨm), and caspase 3/7 activation in HCT-116 cells.

Annexin V/PI staining revealed a dose-dependent increase in apoptosis following 48-hour treatment with complex **1** (Fig. 9a,b). In untreated control cells, the majority of the population remained viable, with minimal Annexin V and PI signal. In contrast, treatment with increasing concentrations of complex **1** resulted in a clear increase in both early (Annexin V^+/PI^-) and late apoptotic (Annexin V^+/PI^+) populations. Quantification showed a progressive increase in the total apoptotic fraction, reaching over 60% at 25 μM, indicating that apoptosis is a significant mode of cell death induced by the compound.

To determine whether mitochondrial dysfunction contributes to this apoptotic phenotype, we evaluated the ΔΨm using the JC-1 dye (Fig. 9c,d). In healthy cells, JC-1 accumulates in the mitochondria, forming red-fluorescent aggregates, whereas in cells with depolarized mitochondria, it remains in a monomeric, green-fluorescent form. Treatment with complex **1** caused a pronounced, dose-dependent shift from red to green fluorescence, indicating loss of ΔΨm. At 25 μM, the depolarization pattern was comparable to that induced by Carbonyl cyanide p-trifluoromethoxyphenylhydrazone (FCCP), a known mitochondrial uncoupler, confirming that complex **1** disrupts mitochondrial integrity.

To assess whether apoptosis proceeded via the intrinsic pathway involving effector caspases, we next examined activation of caspases 3 and 7 using a fluorogenic substrate (Fig. 9e,f). A significant, concentration-dependent increase in caspase 3/7 activity was observed after treatment with complex **1**, with the highest

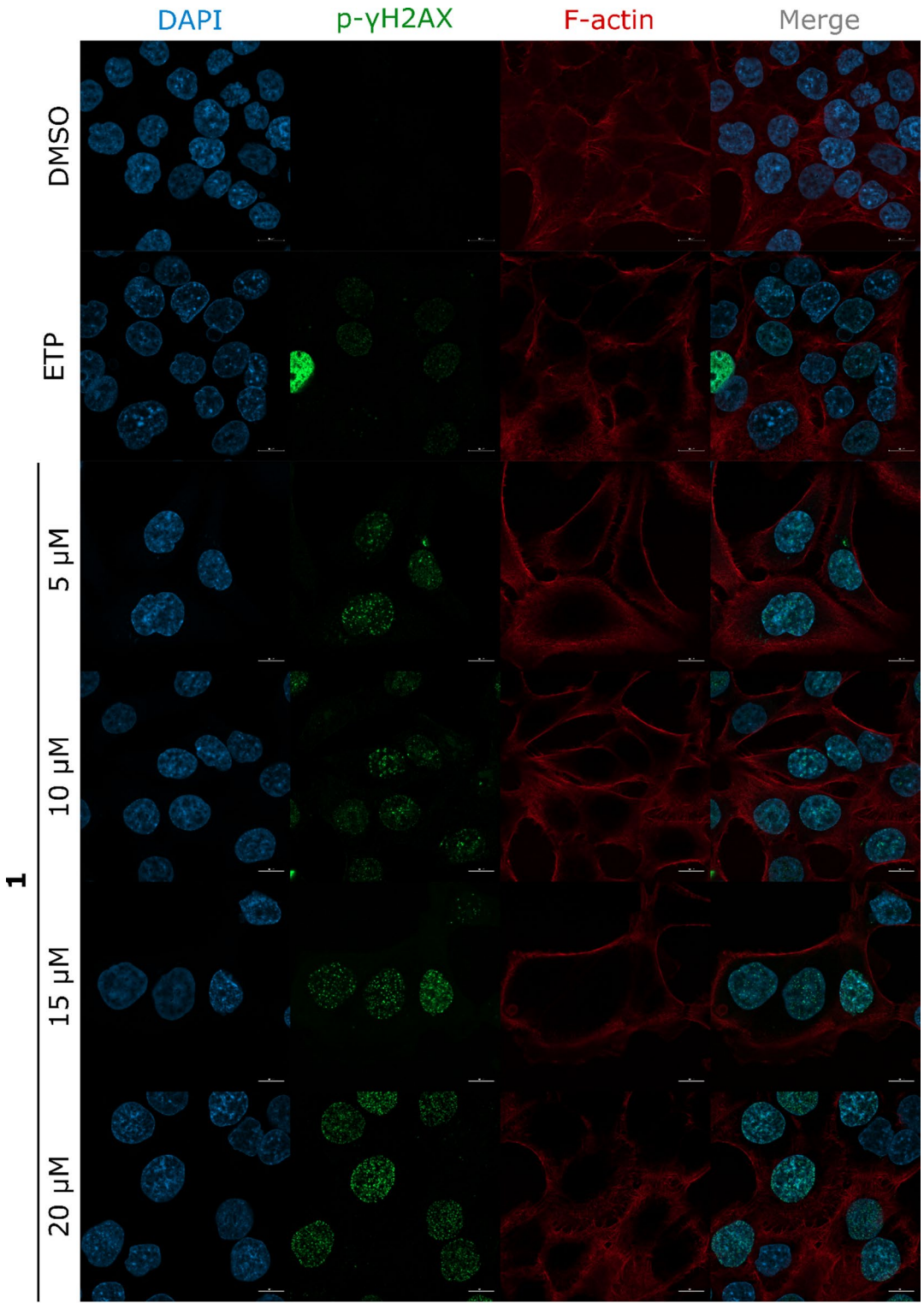

Fig. 8. Confocal microscopy analysis of DNA damage marker γ-H2AX in HCT-116 cells upon treatment with complex **1**. Representative high-resolution images obtained by laser scanning confocal microscopy showing p-γH2AX foci formation (green) and cytoskeletal architecture (F-actin, red) in HCT-116 cells after 48-h treatment with complex **1**. DMSO (vehicle) and **ETP** (positive control) were included as references. Nuclei were counterstained with DAPI (blue). Scale bars = 10 μm.

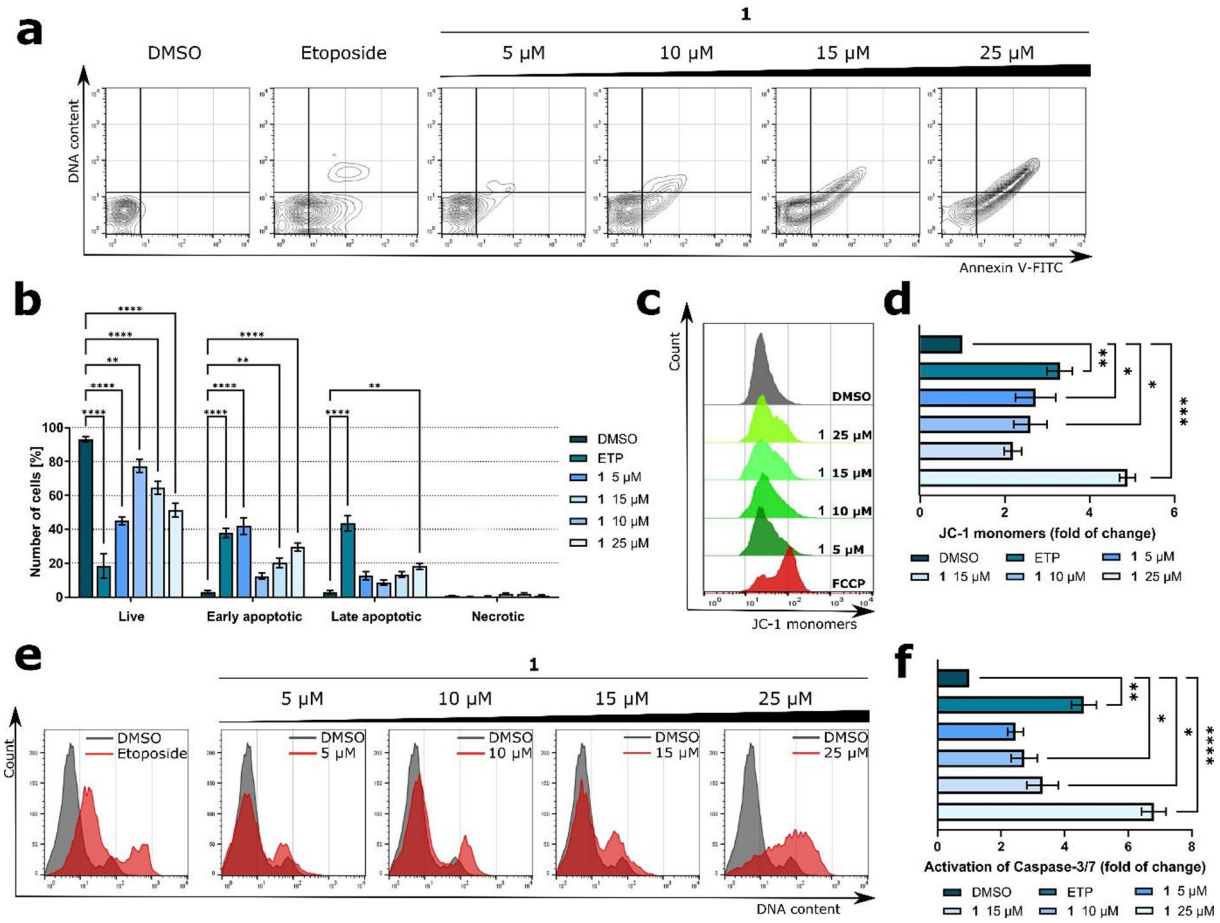

Fig. 9. Proapoptotic activity of complex **1** in HCT-116 cells. (**a**) Representative flow cytometry dot plots showing Annexin V-FITC and 7-AAD staining after 48-hour treatment with complex **1**, **ETP** (positive control), or vehicle (DMSO). (**b**) Quantification of early and late apoptotic cell populations based on Annexin V/7-AAD co-staining. Data represent mean ± SEM from three independent experiments ($n = 3$). (**c**) Representative histograms of JC-1 fluorescence illustrating mitochondrial membrane depolarization after treatment with complex **1** or FCCP (positive control). (**d**) Quantitative analysis of cells with depolarized mitochondrial membrane (JC-1 monomers). (**e**) Representative histograms showing caspase-3/7 activity in HCT-116 cells following 48-hour exposure to complex **1**. (**f**) Quantification of caspase-3/7–positive cells shown as bar graphs (mean ± SEM; $n = 3$). Statistical significance was assessed using two-way ANOVA followed by Dunnett's post hoc test. $^{*}p < 0.01$, $^{**}p < 0.001$, $^{***}p < 0.0001$, $^{****}p < 0.00001$ vs. vehicle-treated control.

activation detected at 25 μM. This response was comparable to that induced by **ETP**, used as a positive control. The histogram overlays and bar charts clearly demonstrate the increase in fluorescence signal corresponding to caspase activation, confirming that complex **1** induces apoptosis through caspase-dependent pathways.

Altogether, these results demonstrate that complex **1** triggers caspase-dependent apoptosis in HCT-116 cells through mitochondrial depolarization and activation of the intrinsic apoptotic pathway, providing further mechanistic insight into its cytotoxic action.

Complex 1 effectively inhibits tumor growth in multicellular spheroids and the chorioallantoic membrane (CAM) assay

To evaluate the antitumor efficacy of complex **1** in a three-dimensional (3D) context, HCT-116-derived multicellular tumor spheroids were generated under low-attachment conditions and exposed to increasing concentrations of the compound (10, 15, 25 and 50 μM). Spheroid morphology was documented, and growth dynamics were monitored over time using brightfield microscopy and real-time imaging (Fig. 10a,b).

In vehicle-treated controls, spheroids exhibited progressive growth and increased compactness over the observation period, reflecting sustained proliferation and preserved structural integrity. In contrast, treatment with complex **1** led to a clear, concentration-dependent inhibition of spheroid expansion. At 10 μM, spheroid growth was modestly reduced, while exposure to 15–50 μM resulted in a pronounced attenuation of surface area increase. Notably, spheroids treated with 50 μM failed to expand and instead exhibited a visible reduction in size and density compared to the baseline. Real-time kinetic monitoring further confirmed the inhibitory effect of complex **1** on proliferative capacity, showing significant divergence from the control growth curves at all tested

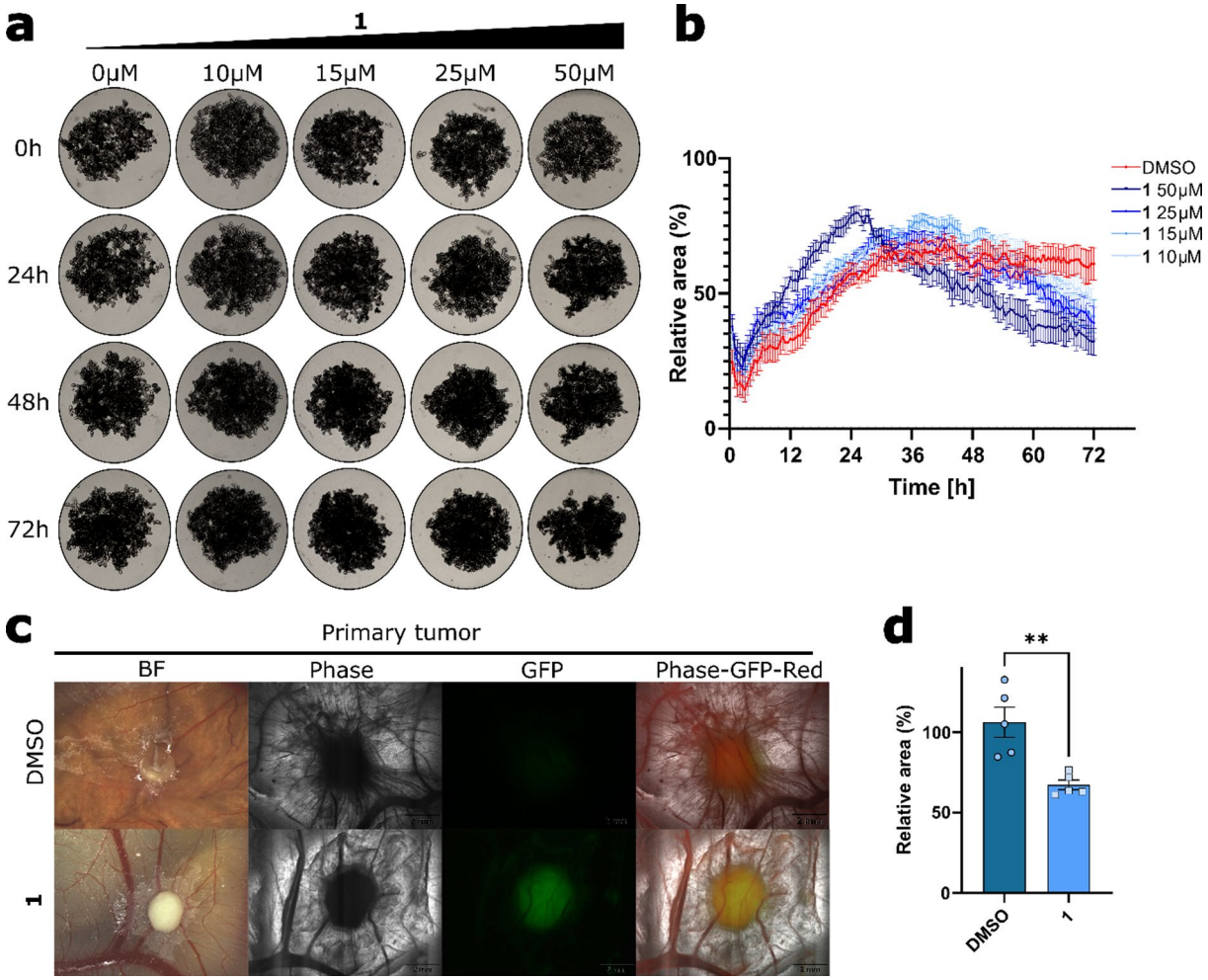

Fig. 10. Antitumor activity of complex **1** in 3D spheroids and CAM models. (**a**) Representative bright-field images of HCT-116 spheroids captured at selected time points during a 72-h incubation with complex **1** at concentrations of 15, 25, or 50 μM, or vehicle (0.5% DMSO). Images show progressive inhibition of spheroids expansion in a concentration-dependent manner. (**b**) Quantitative analysis of spheroids growth presented as percentage change in spheroid area relative to baseline (mean ± SEM; $n = 30$ spheroids per group). (**c**) Representative bright-field and fluorescence images of the chick CAM on embryonic day 14, showing tumors derived from GFP-labeled HCT-116 cells after 48-h treatment with 25 μM **1** or vehicle. Viable tumor cells are visualized by green fluorescence (CellTracker™ Green CMFDA); red vasculature was stained with rhodamine-conjugated Lens culinaris agglutinin (LCA). Scale bar = 2 mm. (**d**) Quantification of tumor-covered area based on fluorescence analysis ($n \geq 5$ tumors per group). Data represent mean ± SEM. Statistical significance was evaluated using one-way ANOVA with Dunnett's post hoc test; $p < 0.001$ vs. control.

concentrations (Fig. 10b). The most severe effects were observed at 50 μM, where spheroids displayed early signs of disaggregation and loss of cohesion, indicating impaired viability and compromised structural organization.

Based on the observed potency in the 3D model, the HCT-116 cell line was selected for subsequent validation in the CAM assay to examine whether the compound's antiproliferative effects extend to an in vivo-like environment. GFP-labeled HCT-116 cells were grafted onto the CAM surface on embryonic day 8 (EDD 8) and allowed to establish vascularized tumors. After four days, complex **1** was applied topically at a concentration of 25 μM, while the control group received vehicle (DMSO) under identical conditions. Treatment was continued for 48 h, after which the tumors were imaged and excised for further analysis (Fig. 10c,d).

In the control group, tumors appeared as dense, vascularized nodules with strong, homogeneous GFP fluorescence, indicating high cell viability and density. In contrast, tumors treated with complex **1** were visibly smaller with notably reduced and heterogeneous fluorescence signals (Fig. 10c,d). These observations suggest substantial impairment of tumor growth and viability in response to the compound. Quantitative analysis of tumor area revealed a statistically significant reduction in size following treatment, with an average decrease of approximately 35% relative to vehicle-treated controls ($p < 0.001$, Fig. 10d). No signs of hemorrhage, necrosis, or detachment from the CAM were observed. Nonetheless, tumors in the treatment group appeared morphologically distinct from controls, displaying a flatter, less compact appearance and lighter coloration.

These differences suggest that the observed effect was likely due to specific inhibition of tumor growth rather than nonspecific toxicity.

Altogether, these results confirm the potent antitumor activity of complex **1** in both 3D spheroids and CAM models. The ability of complex **1** to suppress tumor proliferation in spatially organized and vascularized systems reinforces its potential as a candidate for further preclinical development.

Discussion

Metal-based complexes constitute a promising and increasingly investigated class of anticancer agents due to their unique physicochemical properties and capacity to engage molecular targets through coordination interactions, and potential to overcome drug resistance[39]. Since the introduction of cisplatin and its demonstrated efficacy against a broad spectrum of solid tumors, significant efforts have been directed toward developing next-generation metal-based therapeutics that can overcome the well-documented limitations of platinum drugs, such as systemic toxicity, poor selectivity, and resistance development[40–42]. In this regard, transition metals like ruthenium, copper, gold, and zinc have garnered considerable attention due to their ability to form stable and tunable coordination complexes with pharmacologically active ligands[31,43–45].

Among these, zinc(II) has emerged as a particularly attractive candidate for drug development. It is an essential trace element in human physiology, has a favorable safety profile, and is chemically versatile. Unlike redox-active metals such as Cu(II) or Fe(II), Zn(II) is redox-inert under physiological conditions, which minimizes the risk of oxidative stress in healthy tissues[46,47]. Furthermore, Zn(II)'s coordination properties enable it to stabilize ligand conformations, modulate interactions with biological targets, and alter key pharmacokinetic features, including solubility and lipophilicity[48–50]. Despite these advantages, Zn(II) complexes remain underexplored relative to their platinum and ruthenium counterparts.

In this study, we report the synthesis and the structural characterization of the first Zn(II) complex based on a QTH scaffold—a multifunctional hybrid ligand incorporating three pharmacologically relevant moieties. Crystallographic analysis confirmed that complex **1** adopts a distorted octahedral geometry around Zn(II). Two HL ligands are coordinated in *NNN* tridente manner via quinoline, imine, and thiazole nitrogen atoms. Octahedral geometry is commonly reported for Zn(II) complexes with *N*-donor ligands and is typically associated with high thermodynamic and kinetic stability[51,52]. Tridentate *NNN* coordination mode of ligand **HL** and resulting octahedral geometriy in complex **1** are consistent with earlier reports on biologically active Zn(II) complexes of pyridine-based THs previously published in our group[30,33,34].

Our rationale was twofold: (i) to explore the anticancer potential of QTH ligands, which have been relatively underutilized; and (ii) to assess whether Zn(II) coordination can enhance or confer biological activity. Notably, the free ligand **HL** displayed weak and selective cytotoxicity only in A-549 lung cancer cells. Contrary, complex **1** exhibited an approximately five-fold increase in cytotoxic activity against HCT-116 cells and gained additional potency against HCT-116 colorectal cancer cells, while exhibiting minimal toxicity in non-malignant HEK-293 cells. The absence of activity in MCF-7 and U-2 OS lines suggests a level of tumor-type specificity. Given that HCT-116 cells were the most responsive to complex **1**, all subsequent mechanistic studies in this work were conducted in this colorectal cancer model.

Mechanistic investigations revealed that complex **1** is associated with pronounced S-phase cell cycle arrest, accompanied by significant inhibition of DNA synthesis as evidenced by reduced BrdU incorporation. These findings point toward an interference with replication fork progression or stability, hallmarks of replication stress—a vulnerability frequently exploited in cancer[53].

Evidence consistent with the DNA-damaging potential of complex **1** was provided by the detection of elevated γH2AX levels in HCT-116 cells. High-resolution confocal microscopy confirmed the formation of discrete nuclear γH2AX foci, indicative of double-strand breaks or collapsed replication forks. The observed S-phase arrest together with γH2AX accumulation suggests perturbation of replication dynamics and activation of a DNA damage response, although direct DNA cleavage cannot be concluded without further assays.

These observations are in agreement with our previous studies on related QTH ligands, such as compound **3c**, which induce S-phase arrest and DNA damage in colorectal cancer cells, albeit primarily through modulation of autophagy. Incorporation of Zn(II) into the ligand scaffold, as in complex **1**, appears to potentiate DNA-targeting activity by improving ligand conformation, uptake, and intracellular persistence. Similar mechanistic outcomes—notably S-phase arrest and γH2AX activation—have been reported for other Zn(II) complexes, particularly those based on thiosemicarbazone ligands[54], underscoring the general potential of Zn(II) in designing selective DNA-targeted agents.

In addition to genotoxic effects, complex **1** also induced mitochondrial depolarization, caspase-3/7 activation, and Annexin V positivity, consistent with the initiation of intrinsic apoptosis. Previous reports on Zn(II) complexes have implicated ligand-induced mitochondrial targeting as a driver of apoptosis, supporting the multifaceted cytotoxic mechanism observed here[55,56]. The ability to simultaneously induce replication stress and mitochondrial apoptosis is therapeutically significant, as it could bypass resistance mechanisms associated with traditional apoptosis inducers and exploit cancer-specific metabolic liabilities.

To explore in vivo relevance, we tested complex **1** in both 3D multicellular spheroids and the chick CAM model. In spheroids, the compound inhibited growth in a dose-dependent manner; at higher concentrations, it caused structural disintegration, suggesting effective tissue penetration and activity in a more physiologically relevant context. In the CAM model, complex **1** significantly reduced tumor size and fluorescence without causing overt vascular damage or necrosis, indicating a targeted antitumor effect.

Overall, our findings demonstrate that metal coordination can effectively enhance the biological activity of pharmacologically interesting ligands, transforming them into potent and selective anticancer agents. Unlike classical platinum drugs that act via direct DNA crosslinking, Zn(II)-based complexes, such as the one described here, may exert their effects, at least in part, by modulating the replication machinery and mitochondria-

mediated apoptosis. Zn(II)'s redox-inert and biocompatible nature makes it especially suitable for this purpose, potentially offering improved selectivity and lower toxicity profiles[57,58].

Nonetheless, some limitations remain. The direct molecular targets of complex **1** have not yet been identified, and further studies are needed to determine whether its primary activity is mediated through direct DNA binding, inhibition of replication-associated enzymes, or modulation of DNA repair proteins. Pharmacokinetic profiling, metabolic stability, and mammalian in vivo validation are necessary to fully assess its therapeutic potential. Finally, studies on cellular uptake, for example by ICP-MS, could provide valuable mechanistic insights into intracellular accumulation and optimal exposure times. We therefore highlight such studies as an important direction for future work.

Conclusions

In conclusion, we report the synthesis, structural characterization, and in-depth biological evaluation of the first zinc(II) complex based on a quinoline–thiazolyl–hydrazone scaffold. The complex demonstrates potent and selective anticancer activity against lung and colorectal cancer cells, likely involving mechanisms consistent with replication stress and mitochondrial apoptosis. Its favorable safety profile in normal cells, efficacy in 3D spheroids, and tumor-suppressive activity in the CAM assay support its potential as a promising lead compound for further preclinical development.

These results validate the strategy of metal coordination to enhance the activity and selectivity of pharmacophore-rich ligands, positioning QTH metal complexes as a new chemical space for exploration in targeted anticancer drug discovery.

Methods

Chemistry

Materials and methods

8-Quinolinecarbaldehyde (97%) and 2-bromo-1-(4-methylphenyl)ethan-1-one (97%) were purchased from Maybridge. Thiosemicarbazide (99%) and $Zn(NO_3)_2{\cdot}4H_2O$ (98.5%) were purchased from Acros Organics and Merck, respectively. All employed solvents were of reagent grade and purchased from commercial suppliers. The solvents are used without further purification. Elemental analyses (C, H, N, S) were performed using the standard micro-methods on an ELEMENTAR Vario EL III CHNS/O analyzer. Molar conductivity was measured in DMSO at room temperature (RT) using the Crison Multimeter MM41. IR spectra were recorded in the MID region (4000 –400 cm^{-1}) on a Thermo Scientific Nicolet 6700 FT-IR spectrometer by the Attenuated Total Reflection (ATR) technique. Abbreviations used for IR spectroscopy: vs. (very strong), s (strong), ms (medium strong), m (medium), w (weak), and vw (very weak). The NMR spectra were recorded in DMSO-d_6 using an Agilent 400 instrument. The NMR instruments operate with broad-band direct probes. Tetramethylsilane (TMS) was used as an internal standard for ^1H and ^{13}C, and chemical shifts were given relative to it on the δ scale. Abbreviations used for NMR spectroscopy: s (singlet), d (doublet), dd (doublet of doublets), t (triplet), and m (multiplet). UV–Vis spectrum was recorded in DMSO using LLG-uniSPEC 2 instrument in a wavelength range from 265 to 800 nm. IR, ^1H, and ^{13}C NMR and UV–Vis spectra are shown in Supplementary Figs. S1–S6. The thermal data were collected using a simultaneous thermogravimetric-differential scanning calorimeter, SDT Q600 TA Instruments, under argon (purge flow rate 50 mL/min). The 2.3 mg sample was analyzed in an alumina pan with an empty alumina pan as a reference, from room temperature to 700 °C, at a heating rate of 10 °C/min. The compound's fragmentation during the heating was followed by a HPR20 Hiden Analytical mass spectrometer in scan mode between $m/z = 12$ and $m/z = 93$.

Synthesis of HL

The ligand {2-[8-(quinolyl-2-ylmethylene)hydrazinyl]}-4-(4-tolyl)-1,3-thiazole} (**HL**) was synthesized according to the previously published procedure[1]. The purity of the ligand was confirmed by elemental analysis and NMR spectroscopy.

Synthesis of $[Zn(HL)_2](NO_3)_2$

To a solution of **HL** (0.026 g, 0.0076 mmol) in MeOH (25 cm^3), a solid $Zn(NO_3)_2{\cdot}4H_2O$ (0.01 g, 0.0038 mmol) was added and refluxed for one hour. Yellow single crystals were obtained from the mother liquor after a few days, collected by filtration, and washed with cold methanol, tetrahydrofuran, and diethyl ether. Yield: 76.4 mg (60%). λ_M ($1{\cdot}10^{-3}$ M, DMSO) = 103.55 Ω^{-1} cm^2 mol^{-1}. ^1H NMR (400 MHz, DMSO-d_6): δ_H 2.35 (s, 3H, CH_3), 7.25 (d, 2H, Ar–H), 7.29 (s, 1H, C–$H_{thiazole}$), 7.64 (dd, 1H, Ar–H), 7.74 (t, 1H, Ar–H), 7.79 (d, 2H, Ar–H), 8.06 (d, 1H, Ar–H), 8.33 (d, 1H, Ar–H), 8.46 (dd, 1H, Ar–H), 9.01 (dd, 2H, Ar–H), 9.35 (s, 1H, C–H_{imine}), 12.40 (s, 1H, N–$H_{hydrazone}$). ^{13}C NMR (101 MHz, DMSO-d_6): δ_c 21.22, 103.27, 122.29, 125.04, 125.91, 126.99, 128.51, 129.51, 129.59, 131.75, 132.44, 137.01, 137.23, 138.46, 145.28, 150.66, 151.12, 168.55. IR (ATR, ν_{max}/cm^{-1}): 3083 (s), 2920 (ms), 1622 (vw), 1592 (m), 1579 (ms), 1548 (m), 1498 (vs.), 1381 (vs.), 1326 (ms), 1301 (s), 1260 (ms) 1225 (s), 1120 (ms), 1073 (w), 1035 (w), 949 (w), 938 (w), 921 (w), 910 (w), 871 (w) 836 (w), 824 (m), 791 (m), 767 (m), 717 (w), 683 (w), 655 (w), 633 (w), 602 (w), 587 (w), 529 (w), 512 (w), 489 (w), 472 (w), 456 (vw), 440 (vw), 426 (vw); UV/Vis (DMSO, nm): λ_{max} 285; 385. Analysis (calcd., found for $C_{40}H_{35}N_{10}O_6S_2Zn$ (%)): C (54.70, 54.49), H (3.67, 3.64), N (15.95, 15.64); S (7.30, 7.09).

X-ray crystallography

Data collection of single crystal complexes was performed at RT on a four-circle xtaLAB Synergy Dualflex HyPix diffractometer with the copper anode (Cu Kα, $\lambda = 1.54184$ Å). Data reduction and cell refinement were performed using the CRYSALIS PRO software[59], and the standard multi-scan absorption correction was applied. Structures

were solved by direct methods using SIR2014[60] and refined by a full-matrix least-squares refinement based on F^2 with SHELXL[61]. Hydrogen atoms were either included in their geometrically calculated positions and refined according to the riding model or, in some cases, located in the difference maps. Molecular illustrations were prepared with Mercury (v4.2.1)[62]. Molecular geometries and crystal packing parameters were calculated with PLATON[63]. Single-crystal data, data collection, and refinement parameters are summarized in Supplementary Table S3. 2,469,751 contains the supplementary crystallographic data for **1.** These data can be obtained free of charge *via* http://www.ccdc.cam.ac.uk/conts/retrieving.html or from the Cambridge Crystallographic Data Centre, 12 Union Road, CambridgeCB2 1EZ, UK; fax: (+ 44) 1223-336-033; or e-mail: deposit@ccdc.cam.ac.uk.

Biological evaluation

Cell culture

All cell lines were purchased from ATCC. A-549 (CCL-185) and MCF-7 (HB-8065) were cultured in RPMI-1640 medium, HCT-116 (CVCL-427), and U-2 OS (HTB-96) were cultured in McCoy's 5 A medium, while HEK-293 (CRL-1573) was cultured in DMEM. The culture medium was supplemented by 10% fetal bovine serum, 2 mM L-glutamine, and antibiotics (penicillin 62.6 µg/ml and streptomycin 40 µg/ml) in a humidified atmosphere containing 5% CO_2 at 37 °C and routinely screened for *Mycoplasma* contamination. All reagents, unless stated otherwise, were purchased from Corning.

Drug sensitivity assay

The colorimetric MTT (3,(4,5-dimethylthiazol-2-yl)-2,5-diphenyltetrazolium bromide) assay was used for assessing the cell metabolic activity. Cells were seeded into 96-well plates allowed to attach for 24 h and treated using tested compounds at a concentration of 0–50 µM for 72 h. Etoposide was used as a reference. After treatment, the MTT solution (0.4 mg/ml PBSx1) was added to each well and incubated with cells for an additional 4 h at 37 °C. The culture medium was then removed and the formazan was dissolved in 100 µl of DMSO. The absorbance of samples was measured at 540 nm using an ASYS UVM340 microplate reader (Biochrom Ltd.). The experiment was performed independently, three times. The 72 h incubation period was selected to capture cumulative cytotoxic effects, whereas mechanistic assays (e.g., flow cytometry, apoptosis, immunofluorescence) were conducted after 48 h to detect early cellular responses prior to secondary necrosis.

Flow cytometry

HCT-116 cells were seeded onto Petri dishes and allowed to attach for 24 h. Then, cells were treated with test compounds at various concentration ranges for 48 h. 10 µM **ETP** was used as a reference. The analysis was performed using Guava easyCyte 8 cell sorter (Merck Millipore) and FlowJo v10 software. Each experiment was conducted independently, three times.

Cell cycle

The cells, after treatment with the compounds, were harvested, fixed in ice-cold 75% ethanol, and stored overnight at − 20 °C. The cells were then centrifuged and washed with phosphate-buffered saline (PBS). 20 µg/µl propidium iodide (PI; Sigma-Aldrich) and 100 µg/µl RNaseA (Thermo Fisher) in PBS were used for DNA staining for 20 min at RT.

JC-1 staining

After incubation with the compounds, the culture medium of HCT-116 cells was aspirated and replaced with fresh medium containing 5 µg/ml of JC-1 dye (Sigma-Aldrich). The cells were then incubated in the dark for an additional 20 min at 37 °C. Subsequently, the cells were washed twice with PBS and measured. As a reference 50 µM FCCP (Sigma-Aldrich) was added 15 min before the end of drug treatment.

DNA damage

In brief, treated cells were harvested by trypsinization, fixed in 75% ethanol, and stored overnight or longer at − 20 °C. To detect DNA damage, cells were rinsed with PBS and permeabilized in 0.25% Triton X-100 in PBS for 15 min at RT. The samples were then blocked with 2% bovine serum albumin (BSA) in PBS and incubated with Alexa488- conjugated mouse anti-γH2AX (Ser139) antibody (1:100 BioLegend #613406). 7-AAD (Sigma Aldrich) and 100 µg/µl RNaseA in PBS (20 min, RT) was used for DNA staining).

BrdU incorporation

To assess DNA synthesis, HCT-116 cells were exposed to 20 µM BrdU (Sigma-Aldrich) for 1 h prior to the conclusion of the treatment. Cells were subsequently detached using trypsin and fixed in 75% ethanol at − 20 °C overnight or longer. After fixation, cells were rehydrated in phosphate-buffered saline (PBS) for 10 min and subjected to DNA denaturation with 2 M HCl at room temperature for 45 min. The acidic environment was then neutralized using 0.1 M sodium tetraborate buffer (pH 8.5) for 10 min at room temperature. To minimize non-specific binding, cells were blocked with 1% (w/v) BSA in PBS for 30 min. BrdU incorporation was detected by incubation with a rat monoclonal anti-BrdU antibody (1:100 dilution; Abcam #ab6326) for 1 h at 37 °C, followed by a 30-minute incubation with a goat anti-rat secondary antibody conjugated to a fluorophore (1:200 dilution; Abcam #ab150157). Finally, total DNA was stained using PI (20 µg/ml) in combination with RNase A (100 µg/ml) in PBS for 20 min at room temperature.

Apoptosis and caspase 3/7 staining

HCT-116 cells were harvested by trypsinization, washed two times with PBS, and stained with Annexin V Alexa Fluor™ 488 conjugate (Thermo Fisher, #A13201) for apoptosis assay and with CellEvent™ Caspase-3/7 Green

Flow Cytometry Assay Kit (Thermo Fisher, #C10427) to determine the activation of caspase-3/7 according to the manufacturer's protocols.

Immunofluorescence

HCT-116 cells were seeded on coverslips and allowed to attach for 24 h. After treatment with investigated compounds, cells were washed twice in PBS, fixed with 4% paraformaldehyde (Sigma-Aldrich) in PBS (10 min, RT), and permeabilized for in 0.25% Triton-X100 (Sigma-Aldrich) in PBS (15 min, RT). After permeabilization, samples were rinsed twice with PBS for 5 min each, blocked with 3% BSA (Sigma-Aldrich) in PBS for 1 h at room temperature, and incubated for 1 h at 37 °C with Alexa Fluor 488-conjugated mouse anti-γH2AX (Ser139) antibody (1:250; BioLegend, #613406), diluted in 3% BSA in PBS-T (PBS supplemented with 0.1% (v/v) Tween-20, Sigma-Aldrich). Simultaneously, samples were stained with phalloidin conjugated to a fluorophore (A22287; Thermo Fisher Scientific) to visualize F-actin. After incubation, coverslips were washed twice with PBS-T and counterstained with DAPI (0.25 µg/ml). Imaging was performed using a Zeiss LSM 800 inverted laser scanning confocal microscope equipped with an Airyscan detector and a ×63/1.4 NA Plan-Apochromat objective (Carl Zeiss).

3D spheroid formation assay

Multicellular tumor spheroids were produced using the 3D Petri Dish® system (MicroTissues®, #12-256), following the manufacturer's protocol. A 2% agarose solution in physiological saline was prepared under sterile conditions, liquefied by heating, and dispensed into pre-sterilized micromolds. After cooling and gelation at room temperature, the agarose molds were transferred into standard 12-well plates and equilibrated with complete growth medium. Cells were then seeded into the molds using serum-free medium and allowed to settle by gravity for 1–2 h at 37 °C, enabling even distribution within the microwells. Once cell sedimentation was achieved, culture medium was added to fully submerge the molds and support spheroid development. After the spheroids had formed, they were exposed to the complex **1** at concentrations of 10 µM, 15 µM, 25 µM, or 50 µM, or treated with a 0.5% v/v DMSO in PBS. The spheroids were cultured in a humidified incubator at 37 °C and observed continuously for up to 72 h. Bright-field imaging was performed every 30 min using an Olympus CellVivo inverted microscope equipped for time-lapse live-cell imaging. Spheroid morphology and size changes were quantitatively analyzed using CellSens image analysis software (Olympus). All steps were conducted under aseptic conditions, and each experimental group was tested in a minimum of three independent replicates to ensure reproducibility and statistical reliability.

In ovo CAM assay

The effect of complex **1** on tumor development was assessed using the in ovo CAM model, based on a modified protocol adapted from Rodrigo et al.[64] Fertilized chicken eggs were incubated at 37.5 °C with 65% relative humidity and gentle rotation until embryonic day 8. On the eighth day, a small opening was made in the air sac and a second one above a prominent CAM vessel. Gentle suction was applied to detach the CAM from the eggshell, after which a ~ 1 cm^2 window was cut to access the membrane surface.

HCT-116 cells were pre-stained with CellTracker™ Green (Invitrogen), resuspended in culture medium at a concentration of 4×10^6 cells per 25 µL, and deposited directly onto the CAM in proximity to a visible vascular bifurcation. After a short incubation to ensure cell adherence, the eggs were sealed and returned to the incubator for four additional days to allow tumor formation. On embryonic day 12, tumors were treated with 50 µM **1** dissolved in PBS with 0.5% DMSO. Control eggs received vehicle only. Treatments were carried out over 48 h under static incubation conditions.

To visualize tumor-associated vasculature, LCA (10 µg/mL) was injected into a peripheral CAM vein. The CAM tissues were then excised and fixed in 4% paraformaldehyde (PFA) in PBS. Tumor morphology and vascularization were documented using both stereomicroscopy (Olympus SZX7) and fluorescence microscopy (Olympus IX83) under consistent imaging conditions. Image analysis was conducted in Fiji software, applying background subtraction and threshold-based segmentation to quantify tumor area. A minimum of five independent tumors per group were analyzed under uniform experimental conditions to ensure comparability and data reliability.

As per European Directive 2010/63/EU, the CAM assay is not classified as an animal experiment and does not require ethical approval (reference number: 2021/2784(RSP)).

Data availability

Data will be made available on request.

Received: 2 August 2025; Accepted: 31 October 2025
Published online: 22 November 2025

References

1. Ćurčić, V. et al. Quinoline-based thiazolyl-hydrazones target cancer cells through autophagy inhibition. *Arch. Pharm.* **357**, 2300426. https://doi.org/10.1002/ardp.202300426 (2024).
2. Secci, D. et al. Synthesis of a novel series of thiazole-based histone acetyltransferase inhibitors. *Bioorg. Med. Chem.* **22**, 1680–1689 (2014).
3. Aziz, H. et al. Synthesis, characterization, in vitro tissue-nonspecific alkaline phosphatase (TNAP) and intestinal alkaline phosphatase (IAP) Inhibition studies and computational evaluation of novel thiazole derivatives. *Bioorg. Chem.* **102**, 104088. https://doi.org/10.1016/j.bioorg.2020.104088 (2020).

4. Freitas, L. A. B. et al. Thiazolyl-isatin derivatives: Synthesis, in silico studies, in vitro biological profile against breast cancer cells, mRNA expression, P-gp modulation, and interactions of Akt2 and VIM proteins. *Chem. Biol. Interact.* **394**, 110954. https://doi.org/10.1016/j.cbi.2024.110954 (2024).
5. Fadaly, W. A. A. et al. New pyrazolyl-thiazolidinone/thiazole derivatives as celecoxib/dasatinib analogues with selective COX-2, HER-2 and EGFR inhibitory effects: design, synthesis, anti-inflammatory/anti-proliferative activities, apoptosis, molecular modelling and ADME studies. *J. Enzyme Inhib. Med. Chem.* **38**, 2281262. https://doi.org/10.1080/14756366.2023.2281262 (2023).
6. Omar, A. M. et al. Novel molecular discovery of promising amidine-based thiazole analogues as potent dual matrix Metalloproteinase-2 and 9 inhibitors: anticancer activity data with prominent cell cycle arrest and DNA fragmentation analysis effects. *Bioorg. Chem.* **101**, 103992. https://doi.org/10.1016/j.bioorg.2020.103992 (2020).
7. Sever, B. et al. Design, synthesis, in vitro and in silico investigation of aldose reductase inhibitory effects of new thiazole-based compounds. *Bioorg. Chem.* **102**, 104110. https://doi.org/10.1016/j.bioorg.2020.104110 (2020).
8. Dey, S. et al. Visiblelight-induced ternary electron donor–acceptor complex enabled synthesis of 2-(2-hydrazinyl) thiazole derivatives and the assessment of their antioxidant and antidiabetic therapeutic potential. *Org. Biomol. Chem.* **21**, 1771–1779 (2023).
9. Salar, U. et al. Synthesis, in vitro β -glucuronidase inhibitory activity and in Silico studies of novel (E)-4-Aryl-2-(2-(pyren-1-ylmethylene)hydrazinyl)thiazoles. *Bioorg. Chem.* **70**, 199–209 (2017).
10. Hassan, S. et al. Synthesis of novel (E)-1-(2-(2-(4(dimethylamino) benzylidene) hydrazinyl)-4-methylthiazol-5-yl)ethanone derivatives as ecto-5′-nucleotidase inhibitors. *R Soc. Open. Sci.* **5**, 180837. https://doi.org/10.1098/rsos.180837 (2018).
11. Graser-Loescher, G. et al. Thiosemicarbazone derivatives, Thiazolyl hydrazones, effectively inhibit leukemic tumor cell growth: Down-regulation of ribonucleotide reductase activity and synergism with Arabinofuranosylcytosine. *Food Chem. Toxicol.* **108**, 53–62 (2017).
12. Wang, L. et al. Design, synthesis and biological evaluation of bromophenol-thiazolylhydrazone hybrids inhibiting the interaction of translation initiation factors eIF4E/eIF4G as multifunctional agents for cancer treatment. *E J. Med. Chem.* **177**, 153–170 (2019).
13. Narayanan, S. et al. Anti-cancer effect of Indanone-based Thiazolyl hydrazone derivative on colon cancer cell lines. *Int. J. Biochem. Cell. Biol.* **110**, 21–28 (2019).
14. El-Naggar, A. M., Zidan, A., Elkaeed, E. B., Taghour, M. S. & Badawi, W. A. Design, synthesis and docking studies of new hydrazinyl-thiazole derivatives as anticancer and antimicrobial agents. *J. Saudi Chem. Soc.* **26**, 101488. https://doi.org/10.1016/j.jscs.2022.101488 (2022).
15. Carradori, S. et al. Design, synthesis and biochemical evaluation of novel multi-target inhibitors as potential anti-Parkinson agents. *E J. Med. Chem.* **143**, 1543–1552 (2018).
16. Salem, M. G. et al. Novel 1,3-Thiazole analogues with potent activity against breast cancer: A design, synthesis, in vitro, and in silico study. *Molecules* **27**, 4898. https://doi.org/10.3390/molecules27154898 (2022).
17. Khormi, A. Y. et al. Novel thiazole derivatives incorporating phenyl sulphonyl moiety as potent BRAFV600E kinase inhibitors targeting melanoma. *RSC Adv.* **12**, 27355–27369 (2022).
18. El-Khouly, O. A., Henen, M. A., El-Sayed, M. A. A., Shabaan, M. I. & El-Messery, S. M. Synthesis, anticancer and antimicrobial evaluation of new Benzofuran based derivatives: PI3K inhibition, quorum sensing and molecular modeling study. *Bioorg. Med. Chem.* **31**, 115976. https://doi.org/10.1016/j.bmc.2020.115976 (2021).
19. El-Naggar, A. M., El-Hashash, M. A. & Elkaeed, E. B. Eco-friendly sequential one-pot synthesis, molecular docking, and anticancer evaluation of arylidene-hydrazinyl-thiazole derivatives as CDK2 inhibitors. *Bioorg. Chem.* **108**, 104615 (2021).
20. Piechowska, K. et al. Discovery of tropinone-thiazole derivatives as potent caspase 3/7 activators, and noncompetitive tyrosinase inhibitors with high antiproliferative activity: rational design, one-pot tricomponent synthesis, and lipophilicity determination. *E J. Med. Chem.* **175**, 162–171 (2019).
21. Verma, S., Lal, S., Narang, R. & Sudhakar, K. Quinoline hydrazide/hydrazone derivatives: Recent insights on antibacterial activity and mechanism of action. *ChemMedChem.* **18**, e202200571. https://doi.org/10.1002/cmdc.202200571 (2023).
22. Cardona-G, W., Yepes, A. F. & Herrera, R. Hybrid molecules: promising compounds for the development of new treatments against leishmaniasis and Chagas disease. *Curr. Med. Chem.* **25**, 3637–3679 (2018).
23. Božić, A. et al. Quinoline based mono- and bis-(thio)carbohydrazones: synthesis, anticancer activity in 2D and 3D cancer and cancer stem cell models. *RSC Adv.* **6**, 104763–104781 (2016).
24. Pawar, S., Kumar, K., Gupta, M. K. & Rawal, R. K. Synthetic and medicinal perspective of fused-thiazoles as anticancer agents. *Anticancer Agents Med. Chem.* **21**, 1379–1402 (2021).
25. Evren, A. E., Karaduman, A. B., Sağlik, B. N., Özkay, Y. & Yurttaş, L. Investigation of novel quinoline–thiazole derivatives as antimicrobial agents: in vitro and in silico approaches. *ACS Omega.* **8**, 1410–1429 (2023).
26. Kumar, R. et al. Quinoline-based metal complexes: synthesis and applications. *Coord. Chem. Rev.* **499**, 215453. https://doi.org/10.1016/j.ccr.2023.215453 (2024).
27. Frija, L. M. T., Pombeiro, A. J. L. & Kopylovich, M. N. Coordination chemistry of thiazoles, isothiazoles and thiadiazoles. *Coord. Chem. Rev.* **308**, 32–55 (2016).
28. Podolski-Renić, A. et al. Schiff bases and their metal complexes to target and overcome (multidrug) resistance in cancer. *E J. Med. Chem.* **270**, 116363. https://doi.org/10.1016/j.ejmech.2024.116363 (2024).
29. Erguc, A. et al. Synthesis and biological evaluation of new Quinoline-Based Thiazolyl hydrazone derivatives as potent antifungal and anticancer agents. *LDDD* **15**, 193–202 (2018).
30. Araškov, J. B. et al. Structural insights and photophysical properties of mononuclear and pentanuclear Zn(II) acetate complexes with pyridyl-based thiazolyl-hydrazones. *Polyhedron* **262**, 117162. https://doi.org/10.1016/j.poly.2024.117162 (2024).
31. Pellei, M., Del Bello, F., Porchia, M. & Santini, C. Zinc coordination complexes as anticancer agents. *Coord. Chem. Rev.* **445**, 214088. https://doi.org/10.1016/j.ccr.2021.214088 (2021).
32. Biswas, M., Kanta Choudhury, K., Banerjee, A. & Pathak, R. K. Elevating the discourse on drug delivery: A fresh perspective on the utilization of coordination chemistry-driven metal-drug conjugates. *Coord. Chem. Rev.* **517**, 216026. https://doi.org/10.1016/j.ccr.2024.216026 (2024).
33. Araškov, J. B. et al. Zn(II) complexes with thiazolyl–hydrazones: structure, intermolecular interactions, photophysical properties, computational study and anticancer activity. *CrystEngComm* **24**, 5194–5214 (2022).
34. Araškov, J. B. et al. Structural, physicochemical and anticancer study of Zn complexes with pyridyl-based thiazolyl-hydrazones. *J. Mol. Struct.* **1281**, 135157. https://doi.org/10.1016/j.molstruc.2023.135157 (2023).
35. Elshaflu, H. et al. Co(III) complex with (E)-2-(2-(pyridine-2-ylmethylene)hydrazinyl)-4-(4-tolyl)-1,3-thiazole: structure and activity against 2-D and 3-D cancer cell models. *J. Coord. Chem.* **69**, 3354–3366 (2016).
36. Nakamoto, K. Infrared and Raman spectra of inorganic and coordination compounds. In *Handbook of Vibrational Spectroscopy*. https://doi.org/10.1002/0470027320.s4104 (Wiley, 2006).
37. Montecucco, A. & Biamonti, G. Cellular response to Etoposide treatment. *Cancer Lett.* **252**, 9–18 (2007).
38. Hakala, M. T. Mode of action of 5-bromodeoxyuridine on mammalian cells in culture. *J. Biol. Chem.* **234**, 3072–3076 (1959).
39. Valente, A. et al. Metal- and metalloid-based compounds to target and reverse cancer multidrug resistance. *Drug Resist. Updat.* **58**, 100778. https://doi.org/10.1016/j.drup.2021.100778 (2021).
40. Ghosh, S. Cisplatin: The first metal based anticancer drug. *Bioorg. Chem.* **88**, 102925. https://doi.org/10.1016/j.drup.2021.100778 (2019).

41. Galluzzi, L. et al. Systems biology of cisplatin resistance: past, present and future. *Cell. Death Dis.* **5** (5), e1257. https://doi.org/10.1038/cddis.2013.428 (2014).
42. Kelland, L. The resurgence of platinum-based cancer chemotherapy. *Nat. Rev. Cancer*. **7**, 573–584 (2007).
43. Moreno-Alcántar, G., Picchetti, P. & Casini, A. Gold complexes in anticancer therapy: from new design principles to Particle-Based delivery systems. *Angew Chem. Int. Ed. Engl.* **62**, e202218000. https://doi.org/10.1002/anie.202218000 (2023).
44. Lee, S. Y., Kim, C. Y. & Nam, T. G. Ruthenium complexes as anticancer agents: A brief history and perspectives. *Drug Des. Devel Ther.* **14**, 5375–5392 (2020).
45. Abdolmaleki, S., Aliabadi, A. & Khaksar, S. Riding the metal wave: A review of the latest developments in metal-based anticancer agents. *Coord. Chem. Rev.* **501**, 215579. https://doi.org/10.1016/j.ccr.2023.215579 (2024).
46. Porchia, M., Pellei, M., Del Bello, F. & Santini, C. Zinc complexes with nitrogen donor ligands as anticancer agents. *Molecules* **25**, 5814. https://doi.org/10.3390/molecules25245814 (2020).
47. Lee, S. R. Critical role of zinc as either an antioxidant or a prooxidant in cellular systems. *Oxid. Med. Cell. Longev.* **2018** (9156285), 10115520189156285 (2018).
48. Leuci, R. et al. Importance of biometals as targets in medicinal chemistry: an overview about the role of zinc (II) chelating agents. *Appl. Sci.* **10**, 4118. https://doi.org/10.3390/app10124118 (2020).
49. Munnangi, S. R. et al. Drug complexes: perspective from academic research and pharmaceutical market. *Pharm. Res.* **40**, 1519–1540 (2023).
50. Nagaraj, K. et al. Synthesis, crystal structure, and computational investigation of zinc–cytosine coordination complex: Insights from molecular docking,HOMO-LUMO, and *Appl. Org. Chem.* **39**, e70215. https://doi.org/10.1002/aoc.70215 (2025).
51. Juraj, N. P. & Kirin, S. I. Inorganic stereochemistry: geometric isomerism in bis-tridentate ligand complexes. *Coord. Chem. Rev.* **445**, 214051. https://doi.org/10.1016/j.ccr.2021.214051 (2021).
52. Halder, B. et al. Structural characterization, and theoretical analysis of nonconventional bonding in dinuclear Zinc(II) complexes with tridentate schiff bases. *ACS Omega*. **9**, 41787–41796 (2024).
53. Zeman, M. K. & Cimprich, K. A. Causes and consequences of replication stress. *Nat. Cell. Biol.* **16**, 2–9 (2014).
54. Jiang, M. et al. Development of a zinc(II) 2-pyridinecarboxaldehyde thiosemicarbazone complex with remarkable antitumor and antiangiogenic activities. *Dalton Trans.* **52**, 6029–6040 (2023).
55. Co(II). Cu(II), and Zn(II) thio-bis(benzimidazole) complexes induce apoptosis via mitochondrial pathway. *J. Inorg. Biochem.* **264**, 112786. https://doi.org/10.1016/j.jinorgbio.2024.112786 (2025).
56. Huang, K. B. et al. Isoquinoline derivatives Zn(II)/Ni(II) complexes: crystal structures, cytotoxicity, and their action mechanism. *Eur. J. Med. Chem.* **100**, 68–76 (2015).
57. Gai, S. et al. Anticancer activity and mode of action of Cu(II), Zn(II), and Mn(II) complexes with 5-Chloro-2-N-(2-quinolylmethylene)aminophenol. *Molecules* **28**, 4876. https://doi.org/10.3390/molecules28124876 (2023).
58. Kumar, N., Roopa, Bhalla, V. & Kumar, M. Beyond zinc coordination: bioimaging applications of Zn(II)-complexes. *Coord. Chem. Rev.* **427**, 213550. https://doi.org/10.1016/j.ccr.2020.213550 (2021).
59. CrysAlisPRO Oxford Diffraction /Agilent Technologies UK Ltd, Yarnton, England.
60. Burla, M. C. et al. Crystal structure determination and refinement via SIR2014. *J. Appl. Cryst.* **48**, 306–309 (2015).
61. Sheldrick, G. M. Crystal structure refinement with SHELXL. *Acta Crystallogr. C Struct. Chem.* **71**, 3–8 (2015).
62. Macrae, C. F. et al. Mercury 4.0: from visualization to analysis, design and prediction. *J. Appl. Crystallogr.* **53**, 226–235 (2020).
63. Spek, A. L. Structure validation in chemical crystallography. *Acta Crystallogr. D Biol. Crystallogr.* **65**, 148–155 (2009).
64. Merlos Rodrigo, M. A. et al. Extending the applicability of in ovo and ex ovo chicken chorioallantoic membrane assays to study cytostatic activity in neuroblastoma cells. *Front. Oncol.* **11**, 707366. https://doi.org/10.3389/fonc.2021.707366 (2021).

Acknowledgements

The financial support for the maintenance of research facilities used in these studies from Gdańsk University of Technology by the DEC-2/2021/IDUB/V.6/Si grant under the SILICIUM SUPPORTING CORE R&D FACILITIES "Excellence Initiative—Research University" program is gratefully acknowledged. Computations were carried out using the computers of the Centre of Informatics Tricity Academic Supercomputer & Network. This research was supported by the Ministry of Science, Technological Development and Innovation of Republic of Serbia (Contract numbers: No. 451-03-136/2025-03/200168, 451-03-137/2025-03/200116, 451-03-137/2025-03/200125 and 451-03-136/2025-03/200125) and is in accordance with The 2030 Agenda for Sustainable Development of the United Nations (Goal 3: Good health and well-being, Goal 12: Responsible consumption and production and Goal 17: Partnership for the goals).

Author contributions

Conceptualization: Ideas; formulation or evolution of overarching research goals and aims: N.R.F. and N.M. Data curation: Management activities to annotate, scrub, and maintain research data: N.M., N.R.F., T.T., M.S. Formal analysis: Application of statistical, mathematical, computational, or other formal techniques: N.M., M.O., N.F., A.V. Funding acquisition: Acquisition of financial support for the project: N.M., M.S. and T.T. Investigation: Conducting experiments/data collection: N.M., J.A., M.O., A.V., N.F., M.S., (B) B.H. Methodology: N.M., M.O. Project administration: Management and coordination responsibility for research activity: N.M., M.S., T.T., N.R.F. Resources: Provision of study materials, reagents, patients, etc.: T.T., M.S., N.M. Supervision—Oversight and leadership responsibility: T.T. and N.R.F. Validation: Verification of results/reproducibility: N.M., B.G.; Visualization: Preparation, creation, and presentation of figures/data: N.M., J.A., M.O., N.F., B.B.H. Writing—original draft preparation: N.M., J.A., N.F., B.B.H. Writing review and editing: N.M., N.R.F., T.R.T.

Declarations

Competing interests

The authors declare no competing interests.

Additional information

Supplementary Information The online version contains supplementary material available at https://doi.org/10.1038/s41598-025-27051-4.

Correspondence and requests for materials should be addressed to N.M. or N.F.